# Comparing the performance of different geometries of fixed OWC-type wave energy devices using CFD simulations

Vivek Francis, Martyn Hann, Keri Collins, Aude Mulard, Saishuai Dai, and Deborah Greaves

*Abstract*—**The Oscillating Water Column (OWC) stands out as one of the most promising wave energy converter (WEC) concepts to advance to the stage of full-scale prototype development, and a number of studies have been conducted on it. However, despite the considerable efforts of researchers and developers, this concept has not yet achieved commercial maturity, and there remains a scarcity of knowledge regarding the ideal OWC chamber geometry for efficiently harnessing wave energy. The main objective of this study is to support the development of a floating hybrid OWC – solar energy module planned for deployment within the Maldives. To meet design specifications and ensure manufacturing feasibility, we've opted for a hexagonal chamber geometry for the OWC device. Therefore, this paper presents the set-up, validation, and application of a two-phase incompressible 3D Computational Fluid Dynamics (CFD) model based on the Reynolds-averaged Navier-Stokes (RANS) equations and volume of fluid (VOF) surface capturing scheme approach, for a comparative study on the performance of fixed, detached from the seabed, cylindrical, rectangular, and hexagonal OWC WEC geometries. Simulations seek to evaluate the combined effect of key design parameters and wave conditions on the performance of the OWC device. The findings of this study are expected to assist in optimizing the chamber shapes to achieve maximum efficiency, while also providing significant value for the design, construction, and operation of practical OWC devices.**

*Index Terms*—**CFD Simulation, Oscillating Water Column, Wave Energy.**

## I. Introduction

WAVE energy presents a promising avenue for sustainable energy generation, and amongst the various wave energy converter (WEC) technologies, the Oscillating Water Column (OWC) is generally considered to be a leading candidate for further development. This is evidenced by the fact that, of the few WEC concepts to advance to the full-scale prototype stage, OWCs are the most common [1]. The success of OWC devices stems from their simplicity – both in terms of their structure and principle of operation: it essentially consists of a partially submerged hollow chamber and a power take-off (PTO) system. The oscillation of the water column within the chamber, driven by incoming waves, compresses and decompresses the air column above it causing an airflow through the PTO, and thereby converting wave energy into usable electrical power.

Traditionally, rectangular chambers are commonly used in fixed OWCs, especially in those integrated into coastal structures such as breakwaters or piers (for e.g. the OWCs in the Mutriku harbour breakwater [2] and the OWCs in the breakwater at Civitavecchia [3]), and cylindrical chambers are usually used in floating OWC devices (for e.g. the Spar-buoy OWC [4], the Coaxial-duct OWC [5] and the MoonWEC [6]). However, these conventional OWC chamber shapes may not be optimal for capturing wave energy.

Over the last few decades several analytical, experimental, numerical, and hybrid modelling techniques have been applied in the study of OWC devices. Almost all analytical studies that model wave interactions with OWC devices such as those conducted by McCormick [7] Falcao and Sarmento [8], Evans [9], and Falnes and McIver [10] are based on small-amplitude wave theory. Whilst these approaches work reasonably well when modelling simple OWC device geometries (for e.g., a thin-walled vertical tube or two parallel vertical thin walls), more complex geometries require the application of numerical methods.

Prior to the application of Computational Fluid Dynamics (CFD) based modelling techniques, almost all numerical approaches used to study OWCs were based on potential flow theory, with the resulting equations typically solved by applying the boundary element method (BEM). An extensive review of these can be found in [11]. However, none of these studies account for some of the important nonlinear effects that may occur during wave interactions with OWCs, such as: (i) effects due to fluid viscosity, turbulence and vortex shedding within the OWC chamber; (ii) effects due to air turbulence inside the chamber; (iii) effects associated with large amplitude waves and wave breaking, etc.

Experimental investigations, on the other hand, have

Part of a special issue for ICOE 2024. Original version presented at ICOE 2024.

Manuscript submitted 30 June 2025; Accepted 30 June 2025. Published 13 April 2026.



This paper has been subject to single-blind peer review by a minimum of two reviewers.

V. Francis, M. Hann, K. Collins, and D. Greaves are with the School of Engineering, Computing and Mathematics, University of Plymouth, Drake Circus, Plymouth, PL4 8AA, UK (e-mail: vivek.francis@plymouth.ac.uk).

A. Mulard is with AEON Energy Ltd, 23 Park Royal Road, London, NW10 7JH, UK (e-mail: aude@aeon-energy.com).

S. Dai is with the Department of Naval Architecture, Ocean and Marine Engineering, University of Strathclyde, 16 Richmond St, Glasgow, GL1 1XQ, UK (e-mail: saishuai.dai@strath.ac.uk).

Digital Object Identifier:
https://doi.org/10.36688/imej.8.473-479

largely been conducted for the purpose of validating analytical or numerical models and for studying the effects of different design parameters and wave conditions on the hydrodynamic performance of OWC devices [12]–[16]. Although laboratory experiments offer a closer approximation to the physical phenomena being studied, with increasing complexity and parameters of interest, the financial and time cost of conducting such detailed investigations become prohibitive.

Nowadays, the most widely used numerical approach by researchers to study OWCs—which has also been applied in the present study—is based on the Reynolds-averaged Navier-Stokes (RANS) equations, as it easily overcomes the limitations associated with potential flow-based models. CFD models offer precise control over the input conditions, provide a full description of the flow field, and allow for the testing of different configurations without the use of additional resources. Examples that are most relevant to the present investigation include [17], who characterised the performance of a fixed bottom-detached asymmetric rectangular-shaped OWC device using a 3D incompressible CFD model implemented in OpenFOAM, and [18] in which the effect of wave heights and different PTO damping on the hydrodynamic performance of an offshore-stationary symmetrical OWC consisting of a rectangular chamber was investigated by 3D incompressible STAR-CCM+ based CFD simulations. Along similar lines, and using the same software, the performance of a fixed cylindrical OWC device was examined in [19]. Here, the turbulence has been modelled by the shear stress transport (SST) k- $\omega$ model. A more comprehensive literature review on different OWC devices, their PTO systems, and advances in research related to them is given in [1], [11], and [20].

The motivation for our study is to investigate the possibility of using nonconventional hexagonal chamber shapes in OWC devices, keeping in mind the ease of manufacturability of these shapes to meet certain design requirements. Given that the energy capture efficiency of OWC chambers is strongly linked to their geometric configuration, this research aims to understand how different chamber shapes influence their energy trapping characteristics. To achieve this, we are testing equivalent rectangular, cylindrical, and hexagonal OWC chambers, to evaluate each shape's energy capture potential. Since the manufacturing cost of each of these shapes varies based on the amount of material required and the ease of fabrication, both of which play a significant role in minimising overall construction costs, we aim to determine which chamber shape offers the best balance between efficiency and cost.

## II. The Numerical Model

This study was carried out using the interFoam solver of the open-source CFD software OpenFOAM. It solves the incompressible 3D Navier-Stokes equations for a single Eulerian fluid mixture of two immiscible phases. The solver uses the Finite Volume Method (FVM) for discretizing the governing equations and the Volume of Fluid (VOF) method [21] for free surface tracking.

### A. Governing equations

The governing equations for a Newtonian, incompressible and isothermal fluid are the conservation of mass and momentum equations:

$$\nabla \cdot \mathbf{u} = 0 \tag{1}$$

$$\frac{\partial(\rho \mathbf{u})}{\partial t} + \nabla \cdot (\rho\, \mathbf{u}\mathbf{u}) = -\nabla p + \nabla^2(\mu\, \mathbf{u}) + \rho\, \mathbf{g} \tag{2}$$

where $\mathbf{u} = (u, v, w)$ is the fluid velocity, $\rho$ is the fluid density, $p$ is the pressure, $\mu$ is the dynamic viscosity, $\mathbf{g}$ is the acceleration due to gravity, and $t$ is time. In the single-fluid Eulerian approach, the two immiscible fluids — namely water and air — are treated as a single combined fluid. As explained in [22], the physical properties of this fluid are determined by weighted averages based on the liquid volume fraction, $\alpha$, the distribution of which is modelled by a transport equation having the form:

$$\frac{\partial \alpha}{\partial t} + \nabla \cdot (\mathbf{u}\, \alpha) = 0 \tag{3}$$

The volume fraction $\alpha$ represents the proportion of the fluid within each computational cell, where $\alpha = 1$ indicates a region fully occupied by the water phase, and $\alpha = 0$ indicates a region fully occupied by the air phase. In regions where both phases are present, $\alpha$ takes on a value between 0 and 1. The density and viscosity of the combined fluid in each computational cell is calculated by blending the properties of the two phases according to:

$$\rho = \rho_1 \alpha + \rho_2 (1 - \alpha) \tag{4}$$

$$\mu = \mu_1 \alpha + \mu_2 (1 - \alpha) \tag{5}$$

where the subscripts 1 and 2 represent the water and air phases respectively.

### B. Set-up of the Numerical Wave Tank and the OWC models

Wave generation and absorption in the Numerical Wave Tank (NWT) requires specialized boundary conditions, and in this study it is achieved using the waves2Foam toolbox [23]. In this method, at the domain inlet, boundary conditions and an active sponge layer are specified to generate and absorb the waves based on the chosen wave theory. Within the relaxation zones, a relaxation function, given by

$$\alpha_R = 1 - \frac{e^{\chi_R^{3.5}}}{e - 1} \tag{6}$$

is applied in the following way:

$$\phi = \alpha_R\, \phi_{\text{computed}} + (1 - \alpha_R)\, \phi_{\text{target}} \tag{7}$$

where $\phi$ is either $\mathbf{u}$ or $\alpha$, $\phi_{\text{target}}$ is the prescribed value at the beginning of the relaxation zone, and $\chi_R$ is defined such that $\alpha_R = 1$ at the end of the relaxation zone. In the outlet relaxation zone, $\mathbf{u}_{\text{target}} = 0$, and $\alpha_{\text{target}}$ is based on the still water level (SWL) [23].

The 3D NWT is constructed from 27 rectangular blocks arranged in a 3x3x3 grid, with a central block

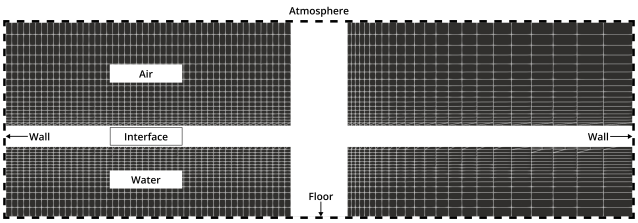


Fig. 1. Mesh topology applied to the NWT. As can be seen, the mesh stretches away from the central block to reduce the total number of cells.

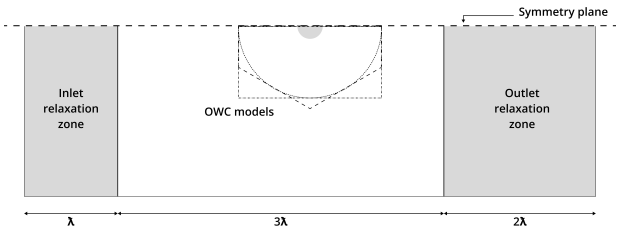


Fig. 2. Schematic of the 3D computational domain and location of the OWC model in the NWT. Figure not to scale.

surrounded uniformly in all directions by neighbouring blocks. The central block consists of a dense mesh made of uniform cubic cells. A cell aspect ratio of 1 is used in this 'working' region. Horizontally, the mesh stretches with distance from the central block to reduce the overall number of cells. Vertically, the mesh is divided into three regions: water, interface, and air. The interface region, where the free surface is most likely to appear during the simulation, has a high cell density. The water region, below the interface, has a moderate mesh density, with the mesh stretching gradually downward to the bottom. The air region, located above the interface, has a lower cell density, with the mesh gradually expanding towards the atmospheric boundary. This meshing strategy is depicted in Fig. 1.

A numerical domain of length $6\lambda$ m ($-3\lambda \leq X \leq 3\lambda$), width 1.53 m ($-0.765 \leq Y \leq 0.765$), and height 1 m ($-0.7 \leq Z \leq 0.3$) is used in all simulations, with the SWL located at $Z = 0$ m. A refinement zone with a thickness of $2H$ is applied around the SWL, ensuring that there are no fewer than 6 cells per $H$ and 222 cells per $\lambda$ (the mesh resolution described here was chosen based on a mesh independence study, as detailed later in the paper). Here, $\lambda$ is the wavelength and $H$ is the height of the simulated wave. The inlet and outlet relaxation zones have lengths of $1\lambda$ m and $2\lambda$ m, respectively (refer Fig. 2), ensuring proper wave generation and absorption. It has been shown previously that an outlet relaxation zone length of more than $0.5\lambda$ provides adequate wave absorption [17], [24]. However, to maintain an extra safe margin, we have used an outlet relaxation zone length of $2\lambda$ m, which is expected to produce negligible reflected waves.

The fixed OWC models tested in the NWT feature three different chamber shapes: cylindrical, rectangular, and hexagonal. All chambers have an inner cross-sectional area of 0.02445 m$^2$ and a thickness of 0.003 m. The cylindrical chamber has an inner diameter of 0.1764 m and a height of 0.1833 m (Fig. 3a). The rectangular chamber shares the same height as the cylinder, with inner dimensions of 0.20 m in length and 0.12225 m in width (Fig. 3b). The hexagonal chamber also matches the height of the others, with an inner side length of 0.097 m (Fig. 3c). All three geometries have a draught of 0.075 m. Each model has a 10 mm diameter orifice, representing the PTO, located on the top cover. The OWC model, imported as a 3D STereoLithography (STL) file, is positioned in the NWT with its centre at $X, Y = 0$, and the $Z$ coordinate aligned with the SWL at device draught. Given the symmetry of the setup, a vertical symmetry plane was applied along the centreline (see Fig. 2), such that only half of the domain needed to be modelled.

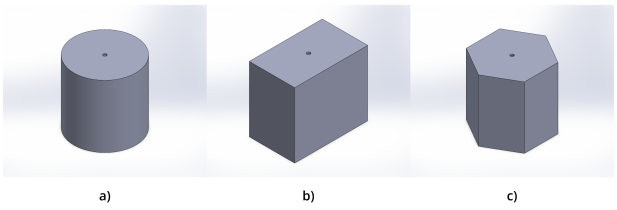


Fig. 3. The different OWC models tested in the NWT.

No-slip and 'zeroGradient' boundary conditions were applied at the bottom of the NWT and along the OWC walls for the velocity and phase fluid fraction respectively, while the top of the domain was defined as an atmospheric pressure boundary. Equations (1) and (2) are solved using a first order temporal scheme (Euler) and second order spatial schemes (Central Differencing and MUSCL [25]). The time step in the simulations is variable and controlled by specifying the maximum value of the Courant number (Co = 0.25), ensuring stability, and the pressure-velocity coupling is achieved through the PIMPLE algorithm using 2 correctors.

Turbulence has been modelled using the $k$–$\omega$ SST model [26]. The $k$–$\omega$ SST model is a two-equation eddy-viscosity model that combines the advantages of both the $k$–$\omega$ [27] and $k$–$\varepsilon$ [28] models. It utilizes the $k$–$\omega$ formulation within the boundary layer, allowing for accurate application up to the walls without requiring damping functions, and transitions to the $k$–$\varepsilon$ formulation in the freestream to mitigate the $k$–$\omega$ model's sensitivity to freestream turbulence properties. The $k$–$\omega$ SST model is particularly effective in handling adverse pressure gradients and flow separation [29], and is the primary reason it was chosen for this study. Furthermore, this turbulence model has been recommended for use in OWC simulations [30], and has also been successfully applied previously to simulate wave interactions with a fixed, detached-from-seabed, cylindrical OWC device [19].

## III. VALIDATION OF THE CFD MODEL

In this section, the validation of the OpenFOAM NWT setup is presented. Initially, we demonstrate the accuracy of wave generation and propagation in a free wave tank (NWT without the OWC model).

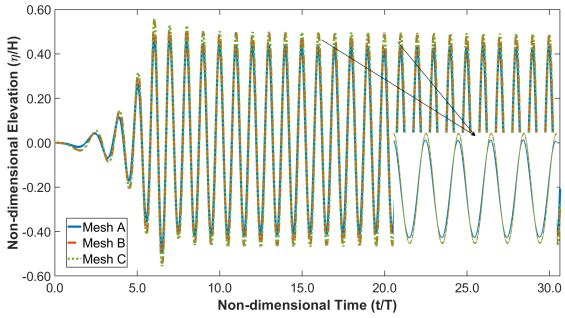


Fig. 4. Time history of the water surface elevations estimated at the middle of the NWT. It can be clearly seen that both Mesh B and Mesh C configurations provide acceptable undamped wave elevations at the location.

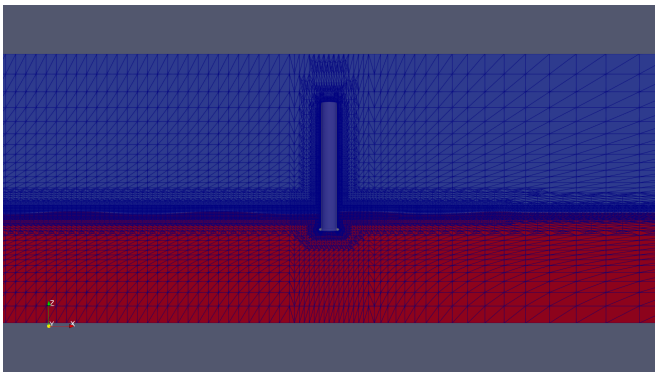

Fig. 5. A 2D view of the 3D CFD domain and overall mesh distribution for the validation simulations. Here, the region in red represents the water phase and the blue denotes air.

This has been done by comparing the wave height (H) and wave period (T) values estimated from the simulations to those of a reference wave. Following this, to validate the CFD model, we recreated the study by Dai et al. [19], where regular wave interactions with a fixed, symmetric, hollow cylinder were investigated. Our numerical predictions of wave elevations inside the cylinder were then compared against their results.

The mesh topology for conducting this validation was developed in two stages: first, an optimised preliminary mesh configuration was established from the free wave tank simulations; subsequently, the final mesh topology was arrived at by refining the preliminary mesh based on Dai et al.'s work, and selecting the resolution that gave the maximum fidelity when compared to their measurements.

### *A. Verification of wave generation and propagation in a free wave tank*

The verification simulations to evaluate wave propagation in the 3D free wave tank were conducted using three different mesh topologies. Each topology featured varying levels of mesh refinement at the free surface: Mesh A had the coarsest resolution (3 cells per $H$ and 133 cells per $\lambda$), Mesh B had a medium resolution (6 cells per $H$ and 222 cells per $\lambda$), and Mesh C had the finest resolution (8 cells per $H$ and 333 cells per $\lambda$).

The reference wave used had a height $H = 0.02$ m, in a constant water depth $d = 0.7$ m, and a wave period $T = 0.766$ s. Stokes fifth-order wave theory was used for generating the wave, and the simulations were run for a duration of $40T$ s. Numerical wave gauges positioned at the middle of the wave tank were used to estimate the surface elevations — this location corresponds to where the OWC device will be centred in our actual simulations. Figure 4 shows the surface wave elevations from the various topologies at the centre of the NWT.

A zero-crossing analysis was conducted to determine the average $H$ and $T$ of the simulated waves and to calculate their relative errors when compared to the target. These results, summarized in the table below, indicate that both Mesh B and Mesh C produce errors within acceptable limits relative to the reference wave ($< 5\%$). To further evaluate the mesh convergence, the grid convergence index (GCI) was calculated for the estimated wave height at the middle of the NWT [31]. The value of $\text{GCI}_{AB}$ (where A indicates a coarse mesh and B the corresponding intermediate mesh) is 5.26%, and $\text{GCI}_{BC}$ (where B again indicates an intermediate mesh and C the corresponding fine mesh) is 3.64%. These values confirm that the estimations are mesh convergent.

Given the need to balance computational efficiency with accuracy, the intermediate Mesh B was selected for conducting the rest of this study as it provides the optimal trade-off between resource demands and numerical precision.

TABLE I
CFD MESHES FOR THE WAVE-PROPAGATION TESTS

| Mesh | Number of cells | Error in $T$ (%) | Error in $H$ (%) |
|---|---|---|---|
| A | 722,394 | $<1$ | 7.5 |
| B | 3,147,404 | $<1$ | 5.0 |
| C | 9,688,440 | $<1$ | 3.5 |

### *B. Comparing with the experimental data of Dai et al. [19]*

Now that confidence has been established in the ability of the NWT to generate waves accurately, the next step is to verify the model's ability to predict wave interactions with structures. To achieve this, a set of 16 simulations were conducted to model regular wave interactions with open-top cylinders, replicating the study by Dai et al [19]. The simulations used monochromatic waves, consistent with those tested by Dai et al., characterised by $H = 0.02$ m, $d = 0.7$ m, and $T$ ranging from $0.593$ s to $1.187$ s. Each simulation was run for a duration of 50 s and the surface elevations, $\eta_{OWC}$, in the middle of the cylinder were sampled.

The Response Amplitude Operators (RAOs) obtained from the CFD model were then compared with the RAOs reported, which were, plotted against Kd (K is the wave number and d is the water depth). The results of this comparison are shown in Fig. 6. It can be clearly seen that the OpenFOAM simulations closely follow the trend and values observed in Dai et al.'s results across the range of Kd, demonstrating good agreement. This strong correlation between the

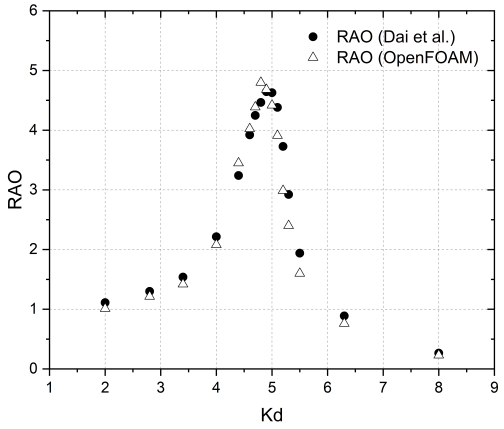


Fig. 6. Comparing the open-top cylinder RAOs obtained from the OpenFOAM model with the results of Dai et al.

RAOs from our CFD model and those reported by Dai et al. confirms the reliability of the numerical setup for simulating wave interactions with structures and lends confidence to the use of the NWT setup for conducting further investigations on OWC models.

## IV. OWC HYDRODYNAMIC EFFICIENCY AND TEST CASES

The period-averaged incident wave power per unit width, $P_{\text{wave}}$ [W/m], can be calculated using the expression:

$$P_{\text{wave}} = \frac{\rho_w g H^2 \omega}{16K}\left(1 + \frac{2Kd}{\sinh(2Kd)}\right) \tag{8}$$

where $\rho_w$ is the density of water, and $\omega$ is the wave frequency. It is important to emphasize that, in this study, for each simulation, the incident wave power has been estimated from free wave tank CFD simulations, based on the water surface elevation, $\eta$, sampled at the location where the OWC device would be. Thus, the incident wave power is computed by excluding the flow perturbations—specifically, the scattering and the reflections—caused by the OWC chamber.

The mean pneumatic power, $P_{\text{OWC}}$ [W], absorbed by the OWC is then determined by integrating the product of air pressure inside the OWC chamber, $p$, and the air flow rate, $q$, over the duration of the analysis window $T_{\text{test}}$ [32]:

$$P_{\text{OWC}} = \frac{1}{T_{\text{test}}}\int_0^{T_{\text{test}}} p \cdot q \, dt \tag{9}$$

In order to directly compare the performance of the different OWC chambers studied, the capture width ratio, CWR, is calculated as:

$$\text{CWR} = \frac{P_{\text{OWC}}}{P_{\text{wave}} W} \tag{10}$$

where $W$ represents the characteristic width of the OWC chamber perpendicular to the wave propagation direction. Here, for the cylindrical and hexagonal OWC devices, $W$ is the outer diameter of the chamber, while for the rectangular chamber, $W$ corresponds to its width.

A hexahedral-dominant mesh was generated around the OWC using the OpenFOAM mesh generation utility `snappyHexMesh`. The mesh is progressively refined towards the OWC walls, with the cell size inside the chamber being approximately 1 mm. Around the top cover of the chamber, the mesh was further refined to accurately capture the orifice geometry, achieving a resolution of around 20 cells per orifice diameter. Additionally, 10 inflation layers with an expansion ratio of 1.15 were added around the OWC walls to achieve a first cell height corresponding to a $Y^+ \approx 1$ near the walls. Once the OWC geometries are meshed, the mesh size is approximately 3 million cells in all cases, with a maximum non-orthogonality of around 65 and a maximum skewness of around 2.3.

The regular waves tested are characterised by $H = 0.02$ m and $T$ ranging between $0.8$ s and $1.2$ s, in a $d$ of $0.7$ m. The simulation duration is set to $20T$, allowing for at least 10 fully developed wave oscillations to occur within the OWC chamber. The surface elevation, $\eta_{\text{OWC}}$, and air pressure, $p$, inside the OWC chamber are sampled at its centre, while the vertical velocity component of the incoming and outgoing air flux, $U_z$, is sampled at the centre of the orifice.

## V. RESULTS AND DISCUSSION

The simulations were carried out using ARCHER2, the UK's National Supercomputing Service, which is based on the Cray EX supercomputing system. For a single simulation run spanning 20T s, the required computational time is approximately 72 hours when executed in parallel across 4 nodes.

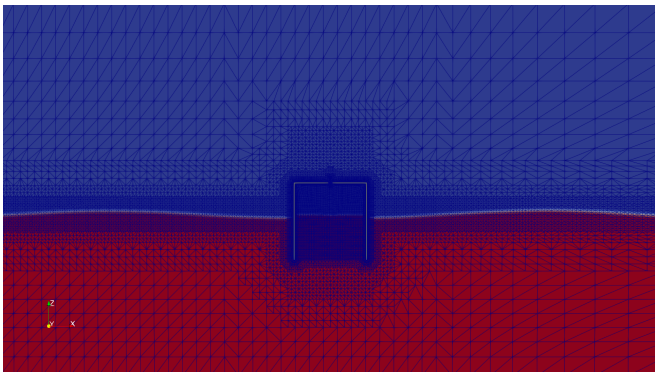

Fig. 7. An overview of the mesh distribution in the OpenFOAM NWT containing the fixed hexagonal cylinder, with the distribution of cells around the OWC device and along the free surface clearly shown.

A comparative analysis of the OpenFOAM model results for $\eta_{\text{OWC}}$, $p$, and $U_z$ across the three chamber geometries was conducted to evaluate their respective performance. The corresponding plots for $T = 0.8$ s are shown in Fig. 9, Fig. 10, and Fig. 11.

For each wave period tested, our incompressible simulation results revealed similar hydrodynamic behaviour across the different tested geometries. The free-surface elevations inside the chambers (Fig. 9) exhibited nearly identical oscillatory patterns, indicating that chamber shape has minimal impact on the wave dynamics. Likewise, the pressure fluctuations in the air

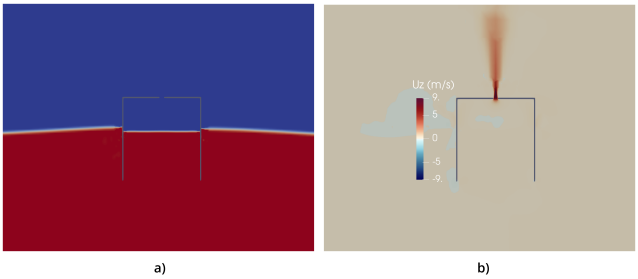


Fig. 8. Cross-sectional view of (a) the water surface elevation and of the (b) vertical component of velocity during the air exhalation phase.

chamber above the water column (Fig. 10) and the vertical velocity through the orifice (Fig. 11) are practically indistinguishable among the three geometries. Small undulations observed in the wave troughs—possibly indicative of sloshing inside the chambers—do not appear to affect pneumatic performance, as reflected in the pressure and velocity plots. These preliminary findings suggest that geometric optimisation of the OWC chamber shape may have only limited impact on device performance.

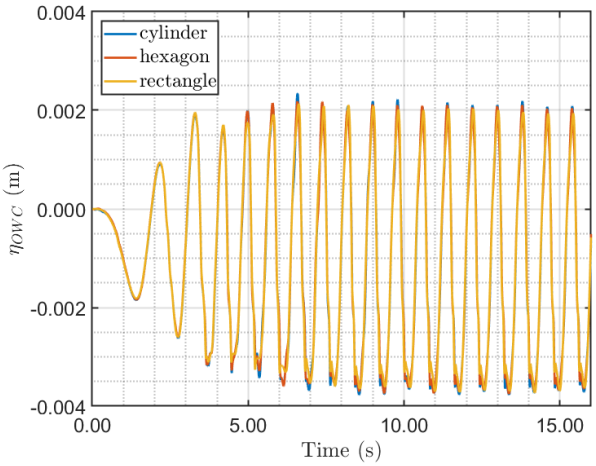


Fig. 9. Time series of the water surface elevations estimated inside the OWC chamber for all three geometries.

The air-flow rate, $q$, can be determined either directly from $U_z$ or indirectly from $\eta_{\mathrm{OWC}}$. Although the latter approach is commonly used, its reliability when there is sloshing inside the chamber—as the piston-like motion of the water column breaks down—is questionable. Therefore, in this study, given the presence of mild undulations in the wave troughs (Fig. 9), we have opted for the former technique. Figure 12 shows the plot of $q$ and the instantaneous power, $IP$, produced within the chamber. For the $T = 0.8$ s, case, the mean pneumatic power, $P_{\mathrm{OWC}}$, is determined to be $0.01$ W, resulting in a capture width ratio, CWR, of $0.19$.

## VI. Conclusions

The present paper describes the verification and validation of a CFD model based on OpenFOAM, developed to study the behaviour of OWC devices. The comparison of our simulation results with previously published experimental data shows excellent agreement, demonstrating the reliability of the approach and showing that the computational flow model is able to adequately account for the physics governing wave interactions with OWC devices.

The primary purpose of this research is to support the development of the AEON floating hybrid OWC – solar energy module, which is planned for deployment

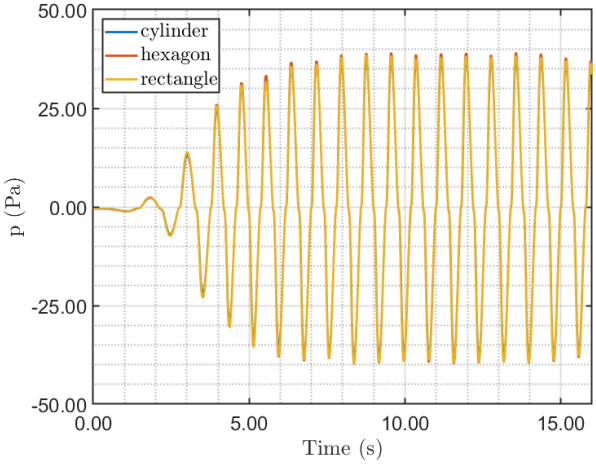


Fig. 10. Time series of the pressure sampled inside the OWC air chamber for all three geometrical shapes tested.

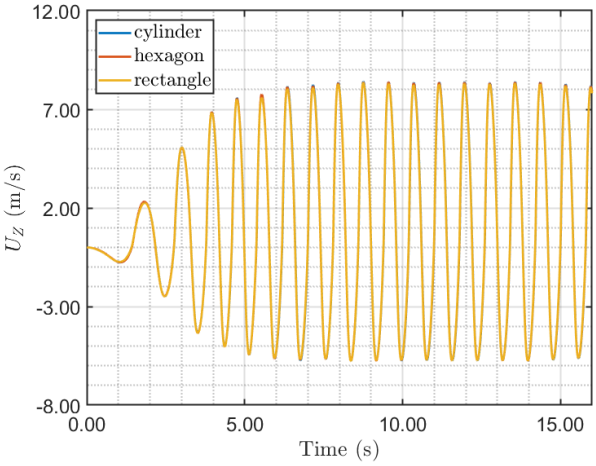


Fig. 11. Time series of the vertical component of air velocity sampled inside the orifice for all three chamber shapes.

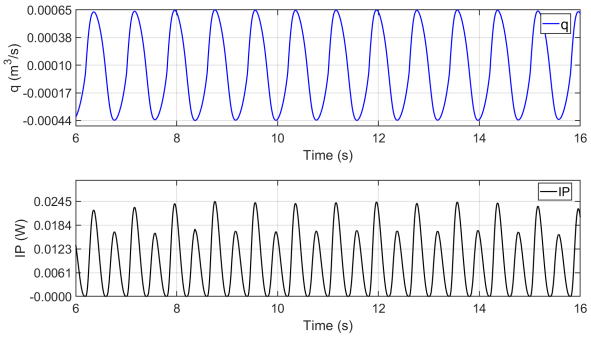


Fig. 12. Time series of the volumetric flow rate (top) and the instantaneous power (bottom) generated in the OWC chamber.

at Ungoofaaru in the Maldives. The specific objective of this study is to identify the optimal geometry for an OWC chamber that maximises power output while minimising manufacturing costs. Instead of allowing the OWC chamber to take any arbitrary shape, we have focussed our investigations on three fundamental geometries with uniform cross-sections: a cylinder, a rectangle, and a hexagon. Our simulation results indicate that there is no significant difference in power output among these different chamber shapes. This suggests that, based on geometric considerations alone, the construction cost of an OWC device can be minimised by choosing a chamber shape that requires less material or is easier to fabricate. For the AEON device, the hexagonal shape meets these criteria.

While this study provides valuable insights, it has to be kept in mind that our approach is not without limitations. For instance, the CFD model used does not account for the compressibility of air. Additionally, further simulations are needed to evaluate and quantify the power performance when key parameters, such as the orientation of the OWC devices with respect to the wave direction, differ from those studied here, and to explore the effects of varied wave spectra, including non-linear and irregular waves. It is also possible that subtle diffraction effects caused by differing chamber shapes could influence the performance of an array of OWCs, and this may warrant further investigation in future studies. However, despite these limitations, the preliminary result of this study gives valuable insights for the planning, design, and construction of practical, real-world OWC devices.

## REFERENCES


[1] A. F. Falcão and J. C. Henriques, "Oscillating-water-column wave energy converters and air turbines: A review," *Renewable energy*, vol. 85, pp. 1391–1424, 2016.

[2] Y. Torre-Enciso, I. Ortubia, L. L. De Aguileta, and J. Marqués, "Mutriku wave power plant: from the thinking out to the reality," in *Proceedings of the 8th European wave and tidal energy conference, Uppsala, Sweden*, vol. 710, 2009, pp. 319–329.

[3] F. Arena, A. Romolo, G. Malara, and A. Ascanelli, "On design and building of a u-owc wave energy converter in the mediterranean sea: a case study," in *International conference on offshore mechanics and Arctic engineering*, vol. 55423. American Society of Mechanical Engineers, 2013, p. V008T09A102.

[4] R. Gomes, J. Henriques, L. Gato, and A. Falcão, "Wave power extraction of a heaving floating oscillating water column in a wave channel," *Renewable Energy*, vol. 99, pp. 1262–1275, 2016.

[5] J. Portillo, J. Henriques, L. Gato, and A. Falcão, "Model tests on a floating coaxial-duct owc wave energy converter with focus on the spring-like air compressibility effect," *Energy*, vol. 263, p. 125549, 2023.

[6] M. A. Khan, G. Barajas, M. G. Gaeta, J. L. Lara, and R. Archetti, "Hydrodynamic analysis and optimization of a floating wave energy converter with moonpool using openfoam®," *Applied Ocean Research*, vol. 142, p. 103847, 2024.

[7] M. E. McCormick, "A modified linear analysis of a wave-energy conversion buoy," *Ocean Engineering*, vol. 3, no. 3, pp. 133–144, 1976.

[8] A. d. O. Falcão, A. Sarmento *et al.*, "Wave generation by a periodic surface pressure and its application in wave-energy extraction," in *15th international congress of theoritical and applied mechanics*, 1980.

[9] D. Evans, "Wave-power absorption by systems of oscillating surface pressure distributions," *Journal of Fluid Mechanics*, vol. 114, pp. 481–499, 1982.

[10] J. Falnes and P. McIver, "Surface wave interactions with systems of oscillating bodies and pressure distributions," *Applied Ocean Research*, vol. 7, no. 4, pp. 225–234, 1985.

[11] V. Baudry, A. Babarit, and A. Clément, "An overview of analytical, numerical and experimental methods for modelling oscillating water columns," in *EWTEC*, 2013.

[12] A. Sarmento, "Wave flume experiments on two-dimensional oscillating water column wave energy devices," *Experiments in fluids*, vol. 12, no. 4, pp. 286–292, 1992.

[13] F. Gouaud, V. Rey, J. Piazzola, and R. Van Hooff, "Experimental study of the hydrodynamic performance of an onshore wave power device in the presence of an underwater mound," *Coastal Engineering*, vol. 57, no. 11-12, pp. 996–1005, 2010.

[14] D.-Z. Ning, R.-Q. Wang, Q.-P. Zou, and B. Teng, "An experimental investigation of hydrodynamics of a fixed owc wave energy converter," *Applied energy*, vol. 168, pp. 636–648, 2016.

[15] T. Vyzikas, S. Deshoulières, M. Barton, O. Giroux, D. Greaves, and D. Simmonds, "Experimental investigation of different geometries of fixed oscillating water column devices," *Renewable energy*, vol. 104, pp. 248–258, 2017.

[16] I. Crema, I. Simonetti, L. Cappietti, H. Oumeraci *et al.*, "Laboratory experiments on oscillating water column wave energy converters integrated in a very large floating structure," in *Proceedings of the 11th European Wave and Tidal Energy Conference, Nantes, France*, 2015, pp. 6–11.

[17] I. Simonetti, L. Cappietti, H. Elsafti, and H. Oumeraci, "Optimization of the geometry and the turbine induced damping for fixed detached and asymmetric owc devices: A numerical study," *Energy*, vol. 139, pp. 1197–1209, 2017.

[18] A. Elhanafi and C. J. Kim, "Experimental and numerical investigation on wave height and power take–off damping effects on the hydrodynamic performance of an offshore–stationary owc wave energy converter," *Renewable energy*, vol. 125, pp. 518–528, 2018.

[19] S. Dai, S. Day, Z. Yuan, and H. Wang, "Investigation on the hydrodynamic scaling effect of an owc type wave energy device using experiment and cfd simulation," *Renewable Energy*, vol. 142, pp. 184–194, 2019.

[20] R. Gayathri, J.-Y. Chang, C.-C. Tsai, and T.-W. Hsu, "Wave energy conversion through oscillating water columns: A review," *Journal of Marine Science and Engineering*, vol. 12, no. 2, p. 342, 2024.

[21] C. W. Hirt and B. D. Nichols, "Volume of fluid (vof) method for the dynamics of free boundaries," *Journal of computational physics*, vol. 39, no. 1, pp. 201–225, 1981.

[22] H. Rusche, "Computational fluid dynamics of dispersed two-phase flow at high phase fractions," *Ph. D. thesis, University of London*, 2002.

[23] N. G. Jacobsen, D. R. Fuhrman, and J. Fredsøe, "A wave generation toolbox for the open-source cfd library: Openfoam®," *International Journal for numerical methods in fluids*, vol. 70, no. 9, pp. 1073–1088, 2012.

[24] S. A. Brown, E. J. Ransley, and D. M. Greaves, "Assessing focused wave impacts on floating wave energy converters using openfoam," *Proceedings of the Institution of Civil Engineers-Engineering and Computational Mechanics*, vol. 174, no. 1, pp. 4–18, 2021.

[25] B. Van Leer, "Towards the ultimate conservative difference scheme. v. a second-order sequel to godunov's method," *Journal of computational Physics*, vol. 32, no. 1, pp. 101–136, 1979.

[26] F. R. Menter, "Improved two-equation k-omega turbulence models for aerodynamic flows," Tech. Rep., 1992.

[27] A. N. Kolmogorov, "Equations of turbulent motion in an incompressible fluid," in *Dokl. Akad. Nauk SSSR*, vol. 30, 1941, pp. 299–303.

[28] B. E. Launder and B. I. Sharma, "Application of the energy-dissipation model of turbulence to the calculation of flow near a spinning disc," *Letters in heat and mass transfer*, vol. 1, no. 2, pp. 131–137, 1974.

[29] A. Elhanafi, A. Fleming, G. Macfarlane, and Z. Leong, "Numerical energy balance analysis for an onshore oscillating water column–wave energy converter," *Energy*, vol. 116, pp. 539–557, 2016.

[30] Y. Zeng, W. Shi, C. Michailides, Z. Ren, and X. Li, "Turbulence model effects on the hydrodynamic response of an oscillating water column (owc) with use of a computational fluid dynamics model," *Energy*, vol. 261, p. 124926, 2022.

[31] P. J. Roache, "Quantification of uncertainty in computational fluid dynamics," *Annual review of fluid Mechanics*, vol. 29, no. 1, pp. 123–160, 1997.

[32] A. Sarmento, "Model-test optimization of an owc wave power plant," *International journal of offshore and polar engineering*, vol. 3, no. 01, 1993.